

Probing Gamma-Ray Burst afterglows with the Cherenkov Telescope Array

Tanima Mondal ¹★, Suman Pramanick ¹†, Lekshmi Resmi ²‡ and Debanjan Bose ³§

¹Department of Physics, Indian Institute of Technology Kharagpur, Kharagpur, West Bengal 721302 India

²Department of Earth & Space Sciences, Indian Institute of Space Science & Technology, Trivandrum 695547, India

³School of Astrophysics, Presidency University, Kolkata 700073, India

Accepted XXX. Received YYY; in original form ZZZ

ABSTRACT

Detection of delayed sub-TeV photons from Gamma-Ray Bursts (GRBs) by MAGIC and HESS has proven the promising future of GRB afterglow studies with the Cherenkov Telescope Array (CTA), the next-generation gamma-ray observatory. With the unprecedented sensitivity of CTA, afterglow detection rates are expected to increase dramatically. In this paper, we explore the multi-dimensional afterglow parameter space to see the detectability of sub-TeV photons by CTA. We use a one-zone electron synchrotron and synchrotron self-Compton model to obtain the spectral energy distribution. We consider bursts going off in a medium of homogenous density. The blast wave is assumed to be radiatively inefficient and evolving adiabatically. Considering that the electron acceleration is not efficient if the acceleration timescale exceeds the radiative cooling timescale, we find that the Sub-TeV emission is always due to the self-Compton process. We find that jets with high kinetic energy or large bulk Lorentz factor decelerating into a dense ambient medium offer better detection prospects for CTA. For relatively lower values of the downstream magnetic field, electrons are slow-cooling, and the emitted radiation is positively correlated with the magnetic field. For larger magnetic fields, the electron population enters the fast cooling phase where the radiated flux is inversely proportional to the magnetic field. We apply our results in the context of bright TeV afterglows detected in recent years. Our results indicate that cosmological short GRBs have only moderate prospects of detection by CTA while local Neutron Star merger counterparts can be detected if the jet is launched towards the observer.

Key words: radiation mechanisms: non-thermal – relativistic processes – methods: numerical – gamma-rays: general – gamma-rays: ISM – gamma-ray bursts.

1 INTRODUCTION

Gamma-ray Bursts (GRBs) release a large amount of energy (10^{49} – 10^{54} erg) in a very short time, known as prompt emission (Klebesadel et al. 1973; Costa et al. 1997; Frontera et al. 1998; van Paradijs et al. 1997; Kulkarni et al. 1999). Thus they are the most powerful explosions in the Universe. GRBs which last for less than 2 seconds are classified as short GRBs, believed to be due to the merger of a binary compact object system involving two Neutron Stars or a Neutron Star and a Black Hole (Eichler et al. 1989; Paczyński 1991; Duncan & Thompson 1992; Usov 1992; Thompson 1994; Metzger et al. 2011). Long GRBs, which last for more than 2 seconds, are believed to be due to the gravitational collapse at the end of a massive star (Woosley 1993; Paczyński 1998; MacFadyen & Woosley 1999; Woosley & Bloom 2006).

A large amount of energy is released predominantly in γ -rays due to dissipative processes inside the ejected material during the prompt emission phase. According to the standard fireball model (Mészáros

& Rees 1992; Meszaros & Rees 1993; Piran et al. 1993; Piran & Shemi 1993; Granot et al. 1999), radiation pressure overcomes gravity and heats matter into a fireball, which then expands relativistically and drives a blast wave through the ambient medium. Afterglow radiation emerges from the kinetic energy of the ejecta dissipated in this medium. Afterglow spectral energy distribution (SED) extends from radio to γ -ray frequencies. Both prompt emission and afterglow arise from non-thermal radiative processes of high-energy particles. See Kumar & Zhang (2015) or Zhang (2018) and references therein for a detailed description of the standard afterglow model explaining both the prompt and afterglow emission.

Currently, a broad picture of the physics of GRBs is established fairly well. However, many finer details, such as the generation of magnetic field and acceleration of high-energy particles by the relativistic shock in its downstream, are still to be understood (Kumar & Barniol Duran 2009; Miceli & Nava 2022; Gill & Granot 2022). In addition, the basic model has failed to reproduce the observed spectral evolution in some well-observed afterglows (Fraija et al. 2022b; Misra et al. 2021; Rhodes et al. 2020). The afterglow phenomena need to be probed in novel ways to fill the gaps in our understanding. Most ($\sim 95\%$) GRBs have well-sampled X-ray afterglow lightcurves, thanks to the fast slewing ability of the Neil Gehrels *Swift* observa-

★ mtanima14@gmail.com

† suman21eor@gmail.com

‡ l.resmi@gmail.com

§ debaice@gmail.com

tery¹. γ -ray afterglows started to get discovered by the launch of *Fermi* satellite², where the Large Area Telescope (LAT)³ started detecting delayed GeV photons in many bursts (Ajello et al. 2019; Tang et al. 2014; Liu et al. 2013).

A novel window of afterglow observations opened up with the recent detections of GeV-TeV photons arriving in timescale of a few minutes since burst, indicating their afterglow origin. Sub-TeV photons from six GRBs⁴ are detected by ground-based Cherenkov telescopes in the last 5 years (Abdalla et al. 2019; Veres et al. 2019; Acciari et al. 2019; Abdalla et al. 2021; Blanch et al. 2020; Huang et al. 2022). The rates will improve with the upcoming Cherenkov Telescope Array (CTA)⁵ (Acharya et al. 2017), and will be opening an unprecedented opportunity for GRB physics.

Afterglow emission arises from non-thermal electrons accelerated by relativistic shocks. These electrons will radiate via synchrotron and Synchrotron Self Compton (SSC) processes. A majority of afterglows observed in radio to X-ray frequencies are due to synchrotron emission by these electrons. For most of the standard parameters, SSC photons start to dominate beyond X-ray or GeV frequencies (Fraija et al. 2019, 2021; Fraija et al. 2022a; Fan et al. 2013; Wang et al. 2019). This means that the SSC component has not been studied observationally as extensively as the synchrotron component until now.

With the LAT and CTA covering the GeV-TeV band, we are now in a position to explore the SSC process in afterglows both observationally and theoretically (Berti et al. 2019). Theoretical predictions of SSC SED can now be tested against the data. No additional parameters enter the problem while modelling the SSC component as the process is self-Compton, not external Compton. Therefore, by probing the new window, a better estimate of the afterglow parameter space, especially the ones governing the shock microphysics, is possible. Since shock microphysics is difficult to predict from the first principles, several simplifying assumptions are used in the standard afterglow model. This is an opportunity to test these assumptions as well, which has already begun (Misra et al. 2021; Rhodes et al. 2020; Veres et al. 2019).

In this paper, we calculate the temporal and spectral evolution of GRB afterglows focusing on the sub-TeV regime to explore GRB afterglow detection probabilities in the era of the CTA. The paper is organized as follows. In section 2, we have discussed our methodology on relativistic blast wave dynamics and time-evolving spectral energy distribution of synchrotron and synchrotron self-Compton (SSC) radiation to obtain VHE GRB afterglow emissions. Extinction of very high energy gamma-ray flux due to EBL (Extra-Galactic Background Light) is discussed in Section 3. In section 4, we have presented light curves and SEDs for a wide range of physical parameters which are likely to be detected by CTA. In section 5, we have shown that our model can explain the VHE afterglow emissions for GRBs detected by ground-based gamma-ray telescopes. Finally, we summarize the paper in section 6.

2 METHODS

In order to obtain the time-evolving afterglow flux from both synchrotron and SSC processes, we have to calculate the time evolution

¹ <https://swift.gsfc.nasa.gov/>

² <https://fermi.gsfc.nasa.gov/>

³ <https://glast.sites.stanford.edu/>

⁴ <http://tevcat.uchicago.edu/>

⁵ <https://www.cta-observatory.org/>

of the magnetic field and electron population downstream. In this section, we describe the dynamics of the relativistic forward shock arising from the interaction of the ejecta with the ambient medium. We have not considered the reverse shock emission in this paper though it is expected to contribute to early emission in the GeV (Fraija et al. 2020).

We consider an ultra-relativistic radially symmetric blast-wave decelerating into a constant density ambient medium. We ignore the lateral expansion phase as it happens in the timescale of a few days for standard afterglow parameters and hence is beyond the reach of VHE telescopes. Since we restrict ourselves to the spherically symmetric initial phase, the opening angle of the jet does not enter the problem. Therefore, the basic parameters are E , the isotropic equivalent kinetic energy in the explosion, n_0 the ambient density, p the power-law index of the non-thermal electron distribution, ϵ_e the fractional thermal energy density in the shock downstream transferred to the non-thermal electrons, and ϵ_B the same transferred to the magnetic field.

The blast wave deceleration is assumed to be adiabatic, i.e., the radiative loss from downstream is considered negligible. To be self-consistent with this assumption, we have assigned a relatively lower fraction of downstream thermal energy in the electron population (see section 2.1).

We consider the simplistic model where the fractional energy in non-thermal electrons and magnetic fields remain constant throughout the evolution. However, there are indications for a deviation from this for TeV bright bursts, particularly (Misra et al. 2021; Rhodes et al. 2020).

2.1 Dynamics

The external forward shock model is based on the interaction of ultra-relativistic ejecta with the ambient medium around the burster. Both the ejecta and the ambient medium are considered to be cold (negligible pressure and temperature) to begin with. The blast wave ahead of the ejected shell decelerates as it transfers energy and momentum to the surrounding medium.

VHE lightcurves typically peak at the early phase of the afterglow, around the beginning of the blast wave deceleration. Therefore, to faithfully reproduce VHE lightcurves, it is important to estimate Lorentz factor evolution at the onset of deceleration accurately. Keeping this in mind, to obtain the afterglow dynamics, we solve the set of ordinary differential equations governing the evolution of the blast-wave Lorentz factor and radius, adopting the treatment by Pe'er (2012).

We begin with the evolution of the bulk Lorentz factor (Γ) of the blast wave as it collects material from the ISM (equation-5 in the original paper),

$$\frac{d\Gamma}{dm} = -\frac{\hat{\gamma}(\Gamma^2 - 1) - (\hat{\gamma} - 1)\Gamma\beta^2}{M + \epsilon m + (1 - \epsilon)m [2\hat{\gamma}\Gamma - (\hat{\gamma} - 1)(1 + \Gamma^{-2})]}, \quad (1)$$

where m is the rest mass of the ambient medium, M is the total mass of the ejected shell, and ϵ is the fractional thermal energy radiated away from the downstream (Huang et al. 1999, 2000).

The adiabatic index ($\hat{\gamma}$) of the downstream plasma is a function of the plasma temperature, which evolves with respect to Γ . As in Pe'er (2012), we use the polynomial fit from Service (1986) to calculate $\hat{\gamma}$ as a function of Γ .

The rest mass of the ambient medium m is given by,

$$dm = 4\pi r^2 \rho dr, \quad (2)$$

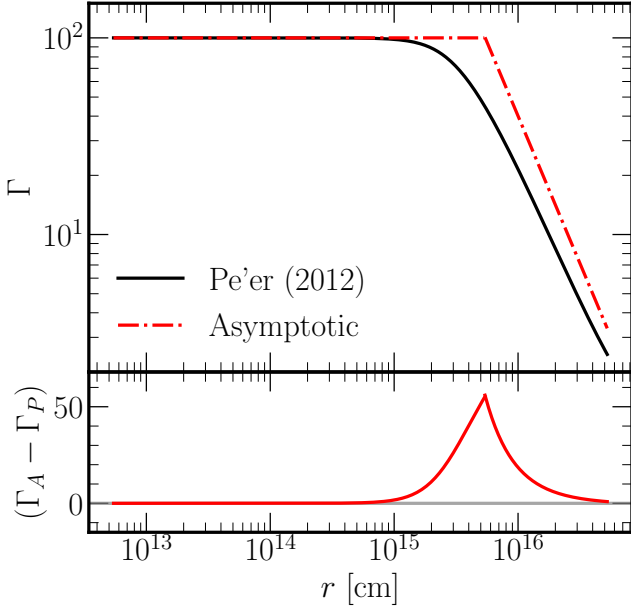


Figure 1. This shows the variation of the bulk Lorentz factor Γ with respect to the blast wave radius r for Pe'er 2012 model (black solid line) and asymptotic solution (red dashed line). The bottom panel (red solid line) shows the difference between the asymptotic (Γ_A) and the Pe'er 2012 (Γ_P) solutions. These plots are generated for $E = 10^{50}$ erg, $\Gamma_0 = 100$ and $n = 10 \text{ cm}^{-3}$.

where r is the radius of the shock front from the explosion site and ρ is the density of the medium.

The photon arrival time (t) for the observer is given by,

$$\frac{dt}{1+z} = dr \frac{(1-\beta)}{\beta c}, \quad (3)$$

where β is the velocity corresponding to the Lorentz factor Γ , z is the cosmological redshift of the source, and c is the speed of light. Here we have assumed the velocity vector to be aligned towards the observer's line of sight.

The three simultaneous ordinary differential equations above describe the evolution of the bulk Lorentz factor of the blast wave as a function of the observer's time. We solve the equations using the ODE solver from the *scipy*⁶ package using the initial condition of $r = 0$, $m = 0$, and $\Gamma = \Gamma_0$. The Lorentz factor decreases as the blast wave starts to decelerate. Analytical approximations consider $\Gamma \propto r^{-3/2}$ for $r > r_{\text{dec}}$ and Γ_0 otherwise, where $r_{\text{dec}} = 10^{18} \text{ cm} (E/10^{52} \text{ erg})^{1/3} n_0^{-1/3} \Gamma_0^{-2/3}$ is the deceleration radius at which the downstream inertial mass is comparable to the mass in the ejecta. n_0 is normalized to 1 cm^{-3} .

In figure 1, we present the evolution of $\Gamma(r)$ from the numerical calculation and the analytical approximation. The difference between the two is shown in the bottom panel. The analytical approximation deviates considerably near the epoch of deceleration where the VHE light curve peaks, leading to an inaccurate estimate of the peak time and the peak flux.

Once $\Gamma(r)$ and $r(t)$ are obtained, we proceed to calculate the synchrotron and SSC flux from the downstream.

2.2 Radiation spectrum

GRB afterglows originate from synchrotron and Synchrotron Self-Compton (SSC) radiation from the blast wave downstream. In this section, we describe the calculation of the time-evolving SEDs of synchrotron and SSC radiation following the framework described in Sari et al. (1998); Wijers & Galama (1999); Panaitescu & Kumar (2000); Sari & Esin (2001). The time evolution of the SED is decided by the dynamics discussed in the previous section.

The first step in calculating the SED is to obtain the energy distribution of non-thermal electrons and the energy density of the magnetic field in the shock downstream.

If the electrons carry a significant fraction of the downstream thermal energy, the blast wave evolution becomes radiative when radiative losses of the electron population are significant (Huang et al. 2000). In such a scenario, one has to consider the transition of the afterglow dynamics from radiative to the adiabatic regime. We assumed a relatively lower ϵ_e to avoid this complication and ensure that radiative losses from the shock downstream are negligible and that the thermal energy density remains intact. For our calculations, we fixed $\epsilon_e = 0.02$.

2.2.1 Synchrotron spectrum

The electrons are distributed as a power-law, specified by the minimum and maximum electron Lorentz factors (γ_m and γ_{max} respectively), and the power-law index p . Using the downstream number density and thermal energy density, γ_m and B can be estimated as $(m_p/m_e)(p-2)/(p-1)\epsilon_e\Gamma$ and $(\epsilon_B 4n_0 m_e c^2)^{1/2}\Gamma$ respectively, where m_p is the rest mass of proton and m_e is the rest mass of electron. We have assumed the entire downstream electrons to be distributed in the non-thermal population.

The injected electron distribution $\propto \gamma^{-p}$ is affected due to energy loss from synchrotron radiation. The comoving timescale $t'_{1/2}$ for an electron to lose half of its initial kinetic energy is given by $(\gamma-1)m_e c^2/P_{\text{syn}}(\gamma)$, where γ is the random Lorentz factor of the electron and $P_{\text{syn}}(\gamma)$ is its total synchrotron power. For a detailed derivation, see Rybicki (2004). At a given time t corresponding to the co-moving time $t' = 2\Gamma t$, electrons with $t'_{1/2} \leq t'$ suffer severe synchrotron losses. The critical Lorentz factor is obtained by equating the two timescales and is given by $\gamma_c^s(t) = \frac{(1+z)6\pi m_e c}{\sigma_T B^2 \Gamma t}$.

Electrons above γ_c^s deviate from the injected power law and settle into a distribution $\propto \gamma^{-(p+1)}$ asymptotically. Therefore, the final synchrotron spectrum can be approximated as piecewise power-law segments separated by $\nu_m = \nu_{\text{syn}}(\gamma_m)$, $\nu_c^s = \nu_{\text{syn}}(\gamma_c^s)$ and $\nu_{\text{max}} = \nu_{\text{syn}}(\gamma_{\text{max}})$, where $\nu_{\text{syn}}(\gamma)$ is the characteristic frequency related to the peak of the single electron synchrotron power and is given by $eB\gamma^2\Gamma/(2\pi m_e c)$. The flux $f_\nu \propto \nu^{1/3}$ if $\nu < \nu_m$, $\nu^{-(p-1)/2}$ if $\nu_m < \nu < \nu_c^s$, and $\nu^{-(p/2)}$ if $\nu_c^s < \nu$. This is valid only for the slow cooling phase ($\gamma_m < \gamma_c^s$).

If all the electrons in the distribution suffer synchrotron losses (fast cooling phase), the distribution function changes to $\propto \gamma^{-2}$ for $\gamma_c^s \leq \gamma < \gamma_m$ and $\propto \gamma^{-(p+1)}$ above γ_m , leading to $f_\nu \propto \nu^{1/3}$ for $\nu < \nu_c^s$, $\nu^{-1/2}$ if $\nu_c^s < \nu < \nu_m$, and $\nu^{-(p/2)}$ if $\nu_m < \nu$.

Electrons can not be accelerated efficiently to Lorentz factors for which the radiative cooling timescale is shorter than the acceleration timescale (Gallant et al. 1999; Achterberg et al. 2001; Dermer & Menon 2009). Therefore, the maximum synchrotron energy can be derived by equating the two timescales. The acceleration timescale is decided by electron confinement in the shock, which in turn is

⁶ www.scipy.org

decided by the gyration radius $r_B = \gamma m_e c^2 / e B$ for an electron of Lorentz factor γ (here, e is the charge of the electron).

Hence, the acceleration timescale in the co-moving frame, $t'_{\text{acc}} = r_B / (e_{\text{acc}} c) = \frac{\gamma m_e c}{e_{\text{acc}} e B}$ (Achterberg et al. 2001; Duran & Kumar 2011; Zhang 2018). e_{acc} is a factor of the order of unity, specific to the acceleration process representing its efficiency.

Comparing t'_{acc} with the synchrotron cooling time, $t'_{1/2} = 6\pi m_e c / \sigma_T B^2 \gamma$ (for $\gamma > 1$), we can derive the maximum synchrotron energy γ_{max} as $\sqrt{6\pi e e_{\text{acc}} / \sigma_T B}$. We fix $e_{\text{acc}} = 0.35$ in our calculations (Zhang et al. 2020a).

2.2.2 Synchrotron Self-Compton spectrum

In order to obtain the radiated power in SSC, first the Compton-Y parameter that relates the seed synchrotron photon field to the upscattered radiation field needs to be calculated. In the regime of Thomson scattering, Y-parameter does not depend on the electron or photon energy, and an asymptotic solution can be given as (Jacovich et al. 2021),

$$Y = \begin{cases} \left(\frac{\epsilon_e}{\epsilon_B} \frac{1}{3-p} \left(\frac{\gamma_m}{\gamma_c} \right)^{p-2} \right)^{\frac{1}{4-p}} & Y \gg 1, \\ \frac{\epsilon_e}{\epsilon_B} \frac{1}{3-p} \left(\frac{\gamma_m}{\gamma_c} \right)^{p-2} & Y \ll 1, \end{cases}$$

for the slow cooling phase. And for the fast cooling phase,

$$Y = \begin{cases} \left(\frac{\epsilon_e}{\epsilon_B} \frac{1}{3-p} \right)^{\frac{1}{4-p}} & Y \gg 1, \\ \frac{\epsilon_e}{\epsilon_B} \frac{1}{3-p} & Y \ll 1. \end{cases}$$

The Y-parameter is also relevant to estimate the cooling Lorentz factor in cases where the total SSC power is greater than the synchrotron power. After including SSC losses, the effective cooling Lorentz factor is modified as $\gamma_c = \gamma_c^s / (1+Y)$. Hence the synchrotron cooling frequency reduces to $\nu_c = \nu_c^s / (1+Y)^2$.

In this paper, we have considered inverse Compton scattering in the Thomson regime, where the scattering is elastic, and the cross-section is insensitive to the energy of the electron or the photon. However, the Klein-Nishina (KN) effect that reduces the scattering cross-section can be significant for photons in the GeV-TeV regime (Fan et al. 2008; Nakar et al. 2009; Wang et al. 2010; Jacovich et al. 2021).

At the time of deceleration, the frequency ν_{KN} above which KN effect becomes significant is given by (Ando et al. 2008),

$$\nu_{\text{KN}} = 41 \text{ GeV} \left(\frac{\Gamma_0}{100} \right)^2 \frac{\epsilon_e}{0.02} \quad \gamma_c < \gamma_m,$$

$$\nu_{\text{KN}} = 3 \text{ TeV} \left(\frac{\Gamma_0}{100} \right)^{2/3} n_0^{-2/3} \left(\frac{\epsilon_B}{10^{-3}} \right)^{-1} (1+Y)^{-1} \quad \gamma_m < \gamma_c.$$

Since most of our analysis is centred around the peak of the 500 GeV lightcurve, we compared $\nu_{\text{KN}}(t_{\text{dec}})$ with 500 GeV. For a part of our parameter space where both ϵ_B and n_0 are large (say, $\gtrsim 10^{-2}$ and $\gtrsim 1.0$ respectively), ν_{KN} can go above 500 GeV. This will reduce the scattering cross-section and therefore decrease the 500 GeV flux. For frequencies 10 times above ν_{KN} , the scattering cross-section drops by a factor of 10 from σ_T and for $\nu = 100\nu_{\text{KN}}$, the drop is ~ 50 .

The characteristic frequencies for the SSC emission are $\nu_m^{\text{SSC}} = 4\gamma_m^2 \nu_m$ and $\nu_c^{\text{SSC}} = 4\gamma_c^2 \nu_c$. We have calculated the SSC spectrum following the prescription Zhang (2018), which is an adaptation of Sari & Esin (2001).

We have ignored optical depth to pair production in obtaining the

SSC spectrum. We have also not considered the effect of γ_{max} as the corresponding frequencies are well above TeV.

In low frequencies, such as in the radio band, synchrotron self-absorption becomes relevant. Though radio photons can be upscattered to γ -ray frequencies, the corresponding flux is too low and often below the synchrotron flux for typical parameters. Therefore, we have not considered synchrotron self-absorption in our calculation and treated the SED to be optically thin always.

3 EBL CORRECTION

Extragalactic Background Light (EBL) is the diffuse electromagnetic radiation that contributes mainly to radiation from stellar nucleosynthesis and radiation from dust after absorbing starlight and AGNs. Radiation from starlight and hot dust mainly contributes to the optical, near-infrared (NIR) and far-infrared (FIR) bands. At the same time, AGNs and quasars are expected to contribute in the mid-IR band no more than 5 – 20% of the total EBL photon density (Matute et al. 2006). Extragalactic backgrounds of other energy bands like radio, UV, X-rays and γ -rays are one to three orders of magnitude smaller than the optical and IR backgrounds (Dole et al. 2006).

The VHE γ -ray photons, which are the main observable frequencies of the ground-based atmospheric Cherenkov telescopes, undergo energy-dependent attenuation due to EBL. VHE γ -ray photons originated from extragalactic sources interact with EBL through pair production (Stecker et al. 1992; Ackermann & Ajello Ackermann & Ajello). This affects the VHE part of the GRB spectrum and changes the shape of the spectrum significantly beyond those energies. A considerable amount of effort has been invested in modelling the EBL attenuation as a function of the energy of the photon and redshift (Franceschini et al. 2008; Finke et al. 2010; Dominguez et al. 2011). These models have been successfully used by several highly sensitive Imaging Atmospheric Cherenkov Telescopes (IACTs) such as MAGIC⁷ (Cortina 2005), HESS⁸ (Hinton et al. 2004) and VERITAS⁹ (Holder et al. 2009), to analyze the observed VHE GRB afterglows from sources of different energies and situated at different redshifts.

The observed flux can be written in terms of the intrinsic flux and the survival probability of the VHE photons as (Hauser & Dwek 2001)

$$\left(\frac{dF}{dE} \right)_{\text{obs}} = \left(\frac{dF}{dE} \right)_{\text{int}} \times e^{-\alpha \tau(E,z)}, \quad (4)$$

where $(dF/dE)_{\text{int}}$ is the intrinsic spectrum of the source, $\tau(E, z)$ is the optical depth of the EBL absorption, which is a function of the energy E and redshift z .

In this paper, we have used the EBL model of Dominguez et al. (2011) and estimate the EBL attenuation factor using a publicly available package JetSet¹⁰ (Massaro et al. 2006; Tramacere et al. 2009, 2011; Tramacere 2020). In the next section, we obtain the EBL-corrected afterglow spectrum and light curves in the CTA frequencies.

⁷ <http://www.magic.iac.es/>

⁸ <https://www.mpi-hd.mpg.de/hfm/HESS/pages/about/telescopes/>

⁹ <https://veritas.sao.arizona.edu/>

¹⁰ Available at: <https://jetset.readthedocs.io/en/1.1.2/>

4 FLUX EVOLUTION IN CTA BANDS

The current statistics of TeV afterglow detections show a diversity in the afterglow behaviour. Therefore, in order to obtain the detectability of GRB afterglows in the GeV-TeV regime, it is important to explore the physical parameter space extensively. See [Galli & Piro \(2008\)](#); [Xue et al. \(2009\)](#); [Fukushima et al. \(2017\)](#); [Vurm & Beloborodov \(2017\)](#); [Zhang et al. \(2020b\)](#); [Joshi & Razzaque \(2021\)](#) for some of the recent explorations in this direction.

The peak flux and the time of peak vary from burst to burst depending on the physical parameters. In addition to the brightness of the afterglow, the timescale in which the afterglow flux remains above the threshold of the detector is also important. For example, the afterglow was detectable for timescales of a few hours in GRB1909114C ([Veres et al. 2019](#)) while it remained above the detection limit for days in the case of GRB190829A ([Abdalla et al. 2021](#)).

4.1 TeV light curve

We consider 500 GeV as a representative frequency to explore the afterglow behaviour in TeV ranges. The reason behind selecting this particular frequency is that it falls in the core energy range of CTA. The sensitivity of CTA is expected to be best in the energy range 100 GeV to 10 TeV ¹¹ ([Bose et al. \(2022\)](#)).

For the entire parameter space we explored, the observed flux in 500 GeV is from the SSC process as $v_{\text{syn}}(\gamma_{\text{max}})$ is below 500 GeV. The deceleration epoch varies from 0.1 to 10 seconds depending on the value of E , n_0 and Γ_0 .

In figures- 3, 4, and 5, we present the light curves in the 500 GeV band for three different redshifts, $z = 0.1, 0.5$, and 1.0 respectively. The left panel is the flux at the source, and the right one is the observed flux after considering EBL attenuation. The vertical lines correspond to analytical approximation of $t_{\text{dec}} = 2.3 \text{sec} E_{51}^{1/3} n_0^{-1/3} (\Gamma_{0,300})^{-8/3}$, where E is normalized to 10^{51} erg, n_0 is normalized to 1 cm^{-3} , and Γ_0 is normalized to 300. As we have used $\Gamma(t)$ from the simultaneous numerical solutions of equations 1, 2 and 3, the light curve peak does not exactly coincide with the analytical value of t_{dec} .

At a given redshift, low E , high Γ_0 , and high n_0 lead to an early deceleration. Therefore an early peak of the light curve, at timescales of the order of a few seconds, can be seen from the figure. Even if detection at such early epochs may be impractical, the peak flux also goes up in case of high E or high n_0 , and the light curve remains above the detection level for a longer period. High values of these parameters are favourable for both detection and follow-up.

At lower redshifts, as the afterglow is brighter, the flux can be detected till about 1000 seconds for most combinations of parameters. However, at the redshift of 1.0, afterglows flux falls below the sensitivity limit after EBL correction, even if the initial bulk Lorentz factor is large.

While the lightcurve peak depends on E , n_0 , and Γ_0 , the peak flux depends on ϵ_B also in addition to these three parameters. The dependence on ϵ_B is visible in the SED at the time of the peak. For all lightcurves presented here, the SED is in the slow cooling regime. Therefore, a larger ϵ_B leads to a larger flux. The correlation reverses for the fast cooling regime (see below).

Next, in order to explore the dependence of the afterglow flux on different parameters, we look at the SEDs of the afterglow.

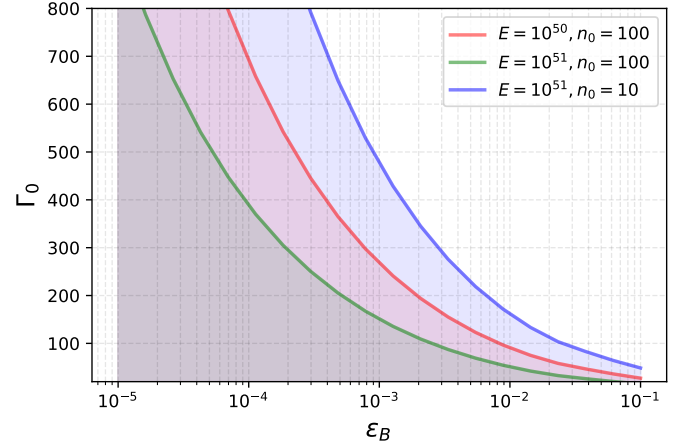


Figure 2. Parameter space deciding electron cooling at t_{dec} . The shaded region corresponds to a slow cooling electron distribution. The region above the line corresponds to fast cooling at t_{dec} . In addition to ϵ_B and Γ_0 , n_0 , E , and ϵ_e are also important in deciding the electron cooling. We fixed $\epsilon_e = 0.02$, redshift $z=0.1$, and considered three different $E - n_0$ pairs in this figure.

4.2 Spectral energy distribution

The peak flux of the light curve depends on a combination of physical parameters. The functional form is decided by the spectral regime in which 500 GeV falls at the time of deceleration.

First, we need to see whether the electrons are in slow or fast cooling regime at t_{dec} . Using the analytical expression for t_{dec} , the factor $\gamma_m/\gamma_c \propto \Gamma_0^{4/3} E^{1/3} n_0^{2/3} \epsilon_e \epsilon_B (1+Y)/(1+z)$ at the peak. Hence, for a fixed ϵ_e , the most important parameters deciding between fast vs slow cooling is ϵ_B and Γ_0 . In figure-2, we present the $\epsilon_B - \Gamma_0$ parameter space at t_{dec} for three different combinations of E and n_0 . For a given ϵ_B , the electrons are in the slow cooling phase if Γ_0 is below a threshold value, which is represented by solid lines in figure-2. The region below the curve represents slow cooling. For a moderate Γ_0 of 300, unless $\epsilon_B > 2 \times 10^{-4}$, the deceleration begins with the electrons in the slow cooling regime and continues to remain so because γ_m drops faster than γ_c post deceleration.

We present SEDs at the peak time for a few representative combinations of physical parameters in figure- 6. The left panels are flux at source, and the right panels are flux corrected for EBL attenuation. The SEDs are for three redshifts, 0.1 and 0.5, and 1.0.

We fixed $\epsilon_e = 0.02$ and $p = 2.2$ in these figures. About 1 GeV or below, the afterglow flux starts to get dominated by SSC. Significant EBL attenuation begins around 300 GeV. For all cases we have presented here, the electrons are in the slow cooling regime. For all of them, $\sqrt{v_m^{\text{SSC}} v_c^{\text{SSC}}} < 500 \text{ GeV} < v_c^{\text{SSC}}$. In this spectral regime, the term $f_{\text{max}}^{\text{SSC}} (v/v_m^{\text{SSC}})^{-(p-1)/2}$ and a logarithmic term consisting of $\log(v_c^{\text{SSC}}/v)$ decide the parameter dependence ([Sari & Esin 2001](#)). Ignoring the contribution from the logarithmic term, an analytical expression for dependencies of physical parameters can be obtained as $f_v^{\text{SSC}} \propto E^{4/3} n_0^{1.467} \Gamma_0^{2.933} \epsilon_B^{0.8} \epsilon_e^{2.4}$. Here, we assumed the analytical expression of t_{dec} .

For relatively higher ϵ_B values, the electrons are fast cooling at the peak time, and v_c^{SSC} goes below 500 GeV. In this regime the parameter dependencies at t_{dec} are $f_v^{\text{SSC}} \propto E^{2/3} n_0^{1/12} \Gamma_0^{-1/3} \epsilon_B^{-5/4}$.

Therefore, the 500 GeV flux is directly proportional to all parameters except ϵ_B in both slow and fast cooling regimes. A higher ϵ_B

¹¹ <https://www.cta-observatory.org/science/cta-performance/>

leads to a higher flux in the slow-cooling regime and a lower flux in the fast-cooling regime (for $500 \text{ GeV} > \min(\nu_m^{\text{SSC}}, \nu_c^{\text{SSC}})$)

4.3 Parameter space favouring TeV detections

In order to fully explore the parameter space determining the lightcurve peak, we generated 500 GeV light curves for a wide range of parameters and obtained the peak flux. We fixed $\epsilon_e = 0.02$ and $p = 2.2$. We varied $10^{49} < E < 10^{51}$ ergs, $0.01 < n_0 < 100 \text{ cm}^{-3}$, $50 < \Gamma_0 < 500$, and $10^{-7} < \epsilon_B < 0.1$. In figures- 7 to 11, we present the observable peak flux after EBL correction against different pairs of parameters to examine the ranges where the afterglow raises above CTA sensitivity. Left-hand side panels correspond to $z = 0.5$ and right-hand side panels are for $z = 0.1$.

As we have seen in figures- 7, 8, 9, higher E , n_0 , and Γ_0 lead to a higher flux. Considering flux for $z = 0.1$ as a proxy for detectability, as EBL attenuation is not significant at that z , for $\epsilon_B = 10^{-3}$ and $\Gamma_0 = 300$, a burst of $E < 10^{51}$ erg is difficult to be detected unless $n_0 > 1$ (see figure-7). The limiting number density reaches ~ 10 and ~ 100 respectively for energy of 10^{50} and 10^{49} ergs. The numbers above correspond to an $\epsilon_B = 0.001$ and $\Gamma_0 = 300$.

The behaviour with ϵ_B is, however different (see figures-10 and 11). During the slow cooling phase (which in turn corresponds to low ϵ_B values), the peak flux increases with ϵ_B . At higher values of ϵ_B the electrons will be in the fast cooling phase. In this phase, if the observed frequency is above ν_c^{SSC} , the lightcurve peak is proportional to $\epsilon_B^{-5/4}$ (see section-4.2). So in the fast-cooling regime, a higher ϵ_B reduces the flux. This can be seen as a change in the direction of the contours in figure-10 and figure-11. Because of this, the peak flux will not increase with ϵ_B beyond a certain threshold. At low E values, therefore, the peak flux can not go beyond a certain limit figure-10.

However, if E or n_0 increases, the value of ϵ_B required for having a fast cooling phase reduces. This is because the magnetic field increases when E , n_0 or ϵ_B increases, forcing γ_c to decrease (see figure-2). The same can be observed in figure-10 and figure-11, as the value at which ϵ_B contours turn direction increases as E or n_0 decreases. Since $\gamma_m/\gamma_c \propto E^{1/3} n_0^{2/3}$, this drift is more visible w.r.t n_0 as in figure-10.

It must be noted that these numbers are for an ϵ_e of 0.02 and $p = 2.2$. For the slow cooling phase, the peak flux is highly sensitive to ϵ_e . The flux $f_V^{\text{SSC}} \propto \epsilon_e^{2(p-1)}$ for $\nu > \nu_m^{\text{SSC}}$, and increase in ϵ_e to 0.1 will lead to an increase in flux by 50 – 100 depending on the value of p . Flux in the fast cooling phase does not depend on ν_m^{SSC} and is insensitive to ϵ_e .

On the other hand, for a higher ϵ_e the fast cooling phase is more likely as discussed in section-4.2, and the above increase is applicable only for relatively lower values of E , n_0 , and Γ_0 .

5 DISCUSSIONS

5.1 Bright TeV afterglows

Since 2018, six Gamma-Ray Bursts are detected in TeV by Cherenkov telescopes (MAGIC, H.E.S.S, and LHAASO). In 2016, A $\sim 3\sigma$ detection is reported for GRB160821B. Of these, GRB190114C, GRB190829A, and GRB221009A were exceptionally bright in TeV with 50, ~ 22 , and $> 100\sigma$ detections respectively. The bursts are at redshifts of 0.424, 0.0785, and 0.151 respectively. Out of these both GRB190114C and GRB221009A had isotropic equivalent energies $E_{\gamma, \text{iso}} > 10^{53}$ ergs in γ -rays. GRB190829A had a relatively

low $E_{\gamma, \text{iso}}$ of $\sim 10^{50}$ erg. Up to 18 TeV photons were detected in GRB221009, which is the first detection of GRBs > 10 TeV.

Our calculations show that at $z = 0.1$, for $E = 10^{50}$ ergs, number densities of $10 - 100 \text{ cm}^{-3}$ and Γ_0 of $100 - 300$ can lead to fluxes $\sim 10^{-11} \text{ erg cm}^{-2} \text{ s}^{-1}$ at $\epsilon_B = 0.001$. Therefore, the detection of TeV photons from GRB190829A is not surprising at $z = 0.0785$.

From figure-6, for $z \sim 0.1$, the afterglow at the peak can be exceptionally bright in 500 GeV depending on other parameters. After an EBL absorption factor of about 0.6, a flux as high as $10^{-10} \text{ erg cm}^{-2} \text{ s}^{-1}$ can be detected in 500 GeV. For all the parameter combinations we presented here, at 10 TeV the flux can reach $\sim 10^{-10} \text{ erg cm}^{-2} \text{ s}^{-1}$ after EBL attenuation correction. For GRB221009A at $z = 0.151$ (de Ugarte Postigo et al. 2022), if all key parameters such as E , n_0 , and Γ_0 are high enough, it is very well possible to detect 10 s of TeV photons at $z \sim 0.1$. Therefore, the detection of 10 TeV photons from nearby GRBs are likely to continue with LHAASO ¹².

5.2 Counterparts of local Neutron Star mergers

Due to the large field of view, CTA can have the potential to detect electromagnetic counterparts from neutron star mergers detected by AdvLIGO/Virgo (Bartos et al. 2014). MAGIC has reported a 3.5σ detection for the LAT detected short GRB160829A (Inoue et al. 2020) at the redshift of 0.424. Short GRBs have relatively lower isotropic equivalent energies as opposed to long GRBs, and they are also likely to happen in low-density surroundings. From figure-7, low kinetic energy jets $< 10^{50}$ launched in low-density medium ($n_0 < 1$) are unlikely to be detectable at $z \sim 0.1$. Therefore, TeV detections of nearby short GRBs are not very promising prospects. However, LIGO detection of nearer ($d_L \sim 200$ Mpc, $z \sim 0.05$) Neutron Star mergers, if associated with a relativistic jet launched towards the observer, the prospects of TeV detections will largely improve. Such a detection will have significant implications in understanding the magnetic field at the shock downstream and the number densities of the surrounding medium.

6 CONCLUSIONS

In this paper, we have explored the sub-TeV emission from GRB afterglows for a range of physical parameters. The optically thin SSC light curve peaks at the epoch of deceleration of the fireball. We focused on the parameter dependence of the peak flux in 500 GeV, considering that as a representative frequency.

If shock acceleration efficiency reduces once the acceleration time scale is larger than the cooling timescale, the 500 GeV lightcurve is solely from the SSC process. We have neglected pair production optical depth and KN effects in calculating the TeV light curve. These can affect our results and reduce the flux by a factor of 10 to 100 for higher n_0 , ϵ_B , and low Γ_0 .

Depending on the physical parameters, particularly on ϵ_B and Γ_0 , the electron population could be in the fast or slow cooling phase at the time of peak. High ϵ_B and low Γ_0 lead to a higher magnetic field and hence a fast cooling population. For an electron population in the slow cooling phase, the peak flux increases with ϵ_B but for a fast cooling population, peak flux decreases with ϵ_B .

In general, afterglows are TeV bright for higher E , n_0 , and Γ_0 . However, nearby bursts with energies $\sim 10^{50}$ ergs, such as GRB190829A,

¹² <http://english.ihep.cas.cn/lhaaso/>

can be detected by Cherenkov telescopes if n_0 or Γ_0 is high enough. Photons of energies as high as 18 TeV were detected in GRB221009 at $z = 0.15$. EBL attenuation at $z \sim 0.1$ can reduce the flux by a factor of 2. From our calculation, we see that if E , n_0 , and Γ_0 are favourable, the high energy photon detection rate by CTA will be promising.

However, because of the lower energy and number densities, CTA detection of GRBs originating from merging neutron stars is not very likely. This will also affect LIGO counterparts from the nearby universe (~ 100 Mpc) if the viewing angles are of the order of a few degrees.

ACKNOWLEDGEMENTS

We thank the anonymous reviewer for his/her thoughtful comments, which have improved the quality of the manuscript. T. Mondal acknowledges the support of the Prime Minister's Research Fellowship (PMRF). T. Mondal like to thank Prof. Sonjoy Majumder, Dept. of Physics, IIT Kharagpur, whose constant guidance has been invaluable. T. Mondal would also like to acknowledge S. Chakraborty, PhD Research Scholar at Dept of Physics, IIT Kharagpur, for his assistance with operating the [Paramshakti Supercomputer facility](#) at IIT Kharagpur—a national supercomputing mission of the Government of India for providing High-Performance Computational resources. S. Pramanick acknowledges the support of [DST-INSPIRE Scholarship](#) and Prime Minister's Research Fellowship (PMRF). L. Resmi acknowledges the Matrics grant MTR/2021/000830 of the Science and Engineering Research Board (SERB) of India. D. Bose acknowledges the support of Ramanujan Fellowship-SB/S2/RJN-038/2017. We use the publicly available package JetSeT to calculate the EBL attenuation factor.

DATA AVAILABILITY

The numerical codes used in this study will be shared upon a reasonable request to the corresponding authors.

REFERENCES

- Abdalla H., et al., 2019, *Nature*, 575, 464
 Abdalla H., et al., 2021, *Science*, 372, 1081
 Acciari V. A., et al., 2019, *Nature*, 575, 455
 Acharya B. S., et al., 2017
 Achterberg A., Gallant Y. A., Kirk J. G., Guthmann A. W., 2001, *Monthly Notices of the Royal Astronomical Society*, 328, 393
 Ackermann M., Ajello M., , *Science*, 338
 Ajello M., et al., 2019, *The Astrophysical Journal*, 878, 52
 Ando S., Nakar E., Sari R., 2008, *Astrophys. J.*, 689, 1150
 Bartos I., et al., 2014, *MNRAS*, 443, 738
 Berti A., et al., 2019, in 36th International Cosmic Ray Conference (ICRC2019), p. 634 ([arXiv:1909.02802](#)), doi:10.22323/1.358.0634
 Blanch O., et al., 2020, GRB Coordinates Network, 29075, 1
 Bose D., Chitnis V. R., Majumdar P., Acharya B. S., 2022, *The European Physical Journal Special Topics*, 231, 3
 Cortina J., 2005, *Astrophysics and Space Science*, 297, 245
 Costa E., et al., 1997, *Nature*, 387, 783
 Dermer C. D., Menon G., 2009, High Energy Radiation from Black Holes: Gamma Rays, Cosmic Rays, and Neutrinos
 Dole H., et al., 2006, *Astronomy & Astrophysics*, 451, 417
 Dominguez A., et al., 2011, *Monthly Notices of the Royal Astronomical Society*, 410, 2556
 Duncan R. C., Thompson C., 1992, *The Astrophysical Journal*, 392, L9
 Duran R. B., Kumar P., 2011, *Monthly Notices of the Royal Astronomical Society*, 412, 522
 Eichler D., Livio M., Piran T., Schramm D. N., 1989, *Nature*, 340, 126
 Fan Y. Z., Piran T., Narayan R., Wei D.-M., Piran T., Narayan R., Wei D. M., 2008, *Mon. Not. Roy. Astron. Soc.*, 384, 1483
 Fan Y.-Z., et al., 2013, *ApJ*, 776, 95
 Finke J. D., Razzaque S., Dermer C. D., 2010, *The Astrophysical Journal*, 712, 238
 Fraija N., Duran R. B., Dichiara S., Beniamini P., 2019, *The Astrophysical Journal*, 883, 162
 Fraija N., Laskar T., Dichiara S., Beniamini P., Duran R. B., Dainotti M., Becerra R., 2020, *The Astrophysical Journal*, 905, 112
 Fraija N., Veres P., Beniamini P., Galvan-Gamez A., Metzger B., Duran R. B., Becerra R., 2021, *The Astrophysical Journal*, 918, 12
 Fraija N., Dainotti M. G., Ugale S., Jyoti D., Warren D. C., 2022a, *ApJ*, 934, 188
 Fraija N., Galvan-Gamez A., Kamenetskaia B. B., Dainotti M. G., Dichiara S., Veres P., Becerra R. L., do ES Pedreira A. C., 2022b, *The Astrophysical Journal*, 940, 189
 Franceschini A., Rodighiero G., Vaccari M., 2008, *Astronomy & Astrophysics*, 487, 837
 Frontera F., et al., 1998, *Astrophys. J. Lett.*, 493, L67
 Fukushima T., To S., Asano K., Fujita Y., 2017, *ApJ*, 844, 92
 Gallant Y., Achterberg A., Kirk J., 1999, *Astronomy and Astrophysics Supplement Series*, 138, 549
 Galli A., Piro L., 2008, *A&A*, 489, 1073
 Gill R., Granot J., 2022, *Galaxies*, 10, 74
 Granot J., Piran T., et al., 1999, *The Astrophysical Journal*, 513, 679
 Hauser M. G., Dwek E., 2001, *Ann. Rev. Astron. Astrophys.*, 39, 249
 Hinton J., et al., 2004, *New Astron. Rev.*, 48, 331
 Holder J., et al., 2009, in AIP Conference Proceedings. pp 657–660, doi:10.1063/1.3076760
 Huang Y. F., Dai Z. G., Lu T., 1999, *Mon. Not. Roy. Astron. Soc.*, 309, 513
 Huang Y. F., Gou L. J., Dai Z. G., Lu T., 2000, *Astrophys. J.*, 543, 90
 Huang Y., Hu S., Chen S., Zha M., Liu C., Yao Z., Cao Z., Experiment T. L., 2022, GRB Coordinates Network, 32677, 1
 Inoue S., et al., 2020, *PoS, ICRC2019*, 703
 Jacovich T. E., Beniamini P., Van Der Horst A. J., 2021, *Mon. Not. Roy. Astron. Soc.*, 504, 528
 Joshi J. C., Razzaque S., 2021, *MNRAS*, 505, 1718
 Klebesadel R. W., Strong I. B., Olson R. A., 1973, *The Astrophysical Journal*, 182, L85
 Kulkarni S. R., et al., 1999, *Nature*, 398, 389
 Kumar P., Barniol Duran R., 2009, *MNRAS*, 400, L75
 Kumar P., Zhang B., 2015, *Physics Reports*, 561, 1
 Liu R.-Y., Wang X.-Y., Wu X.-F., 2013, *ApJ*, 773, L20
 MacFadyen A., Woosley S., 1999, *The Astrophysical Journal*, 524, 262
 Massaro E., Tramacere A., Perri M., Giommi P., Tosti G., 2006, *Astronomy & Astrophysics*, 448, 861
 Matute I., La Franca F., Pozzi F., Gruppioni C., Lari C., Zamorani G., 2006, *Astronomy & Astrophysics*, 451, 443
 Mészáros P., Rees M., 1992, *Monthly Notices of the Royal Astronomical Society*, 257, 29P
 Meszaros P., Rees M., 1993, *The Astrophysical Journal*, 405, 278
 Metzger B., Giannios D., Thompson T., Bucciantini N., Quataert E., 2011, *Monthly Notices of the Royal Astronomical Society*, 413, 2031
 Miceli D., Nava L., 2022, *Galaxies*, 10, 66
 Misra K., et al., 2021, *Monthly Notices of the Royal Astronomical Society*, 504, 5685
 Nakar E., Ando S., Sari R., 2009, *ApJ*, 703, 675
 Paczynski B., 1991, *Acta Astron.*, 41, 257
 Paczyński B., 1998, *The Astrophysical Journal*, 494, L45
 Panaitescu A., Kumar P., 2000, *The Astrophysical Journal*, 543, 66
 Pe'er A., 2012, *The Astrophysical Journal Letters*, 752, L8
 Piran T., Shemi A., 1993, *The Astrophysical Journal*, 403, L67
 Piran T., Shemi A., Narayan R., 1993, *Monthly Notices of the Royal Astronomical Society*, 263, 861

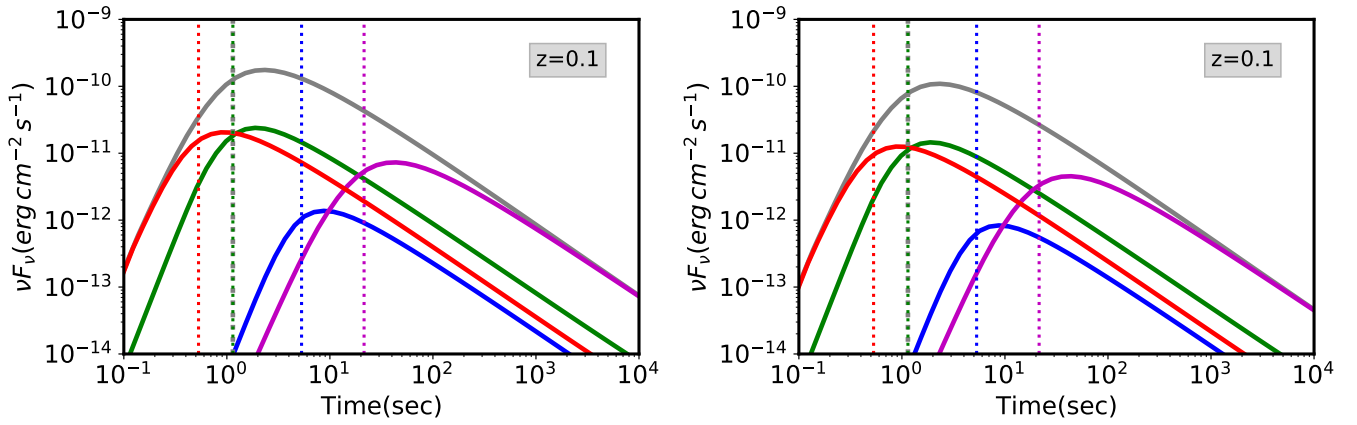


Figure 3. SSC Flux as a function of time is plotted for different combinations of microphysical parameters for redshift $z = 0.1$, we set grey coloured lightcurve as the reference once $[E = 10^{51}\text{erg}, \Gamma_0 = 300, n_0 = 10, \epsilon_B = 10^{-3}]$. Blue, green, magenta and red coloured lines show the lightcurves for parameters $[E = 10^{51}\text{erg}, \Gamma_0 = 300, n_0 = 0.1, \epsilon_B = 10^{-3}]$, $[E = 10^{51}\text{erg}, \Gamma_0 = 300, n_0 = 10, \epsilon_B = 10^{-5}]$, $[E = 10^{51}\text{erg}, \Gamma_0 = 100, n_0 = 10, \epsilon_B = 10^{-3}]$, $[E = 10^{50}\text{erg}, \Gamma_0 = 300, n_0 = 10, \epsilon_B = 10^{-3}]$ respectively, at some fixed parameters $p = 2.2, \epsilon_e = 0.02$ at redshift $z = 0.1$. The lightcurve plot of the left-side panel represents SSC Flux without EBL correction, and the right-side panel depicts the SSC flux with EBL correction by EBL Dominguez factor = 0.6013 at 500 GeV.

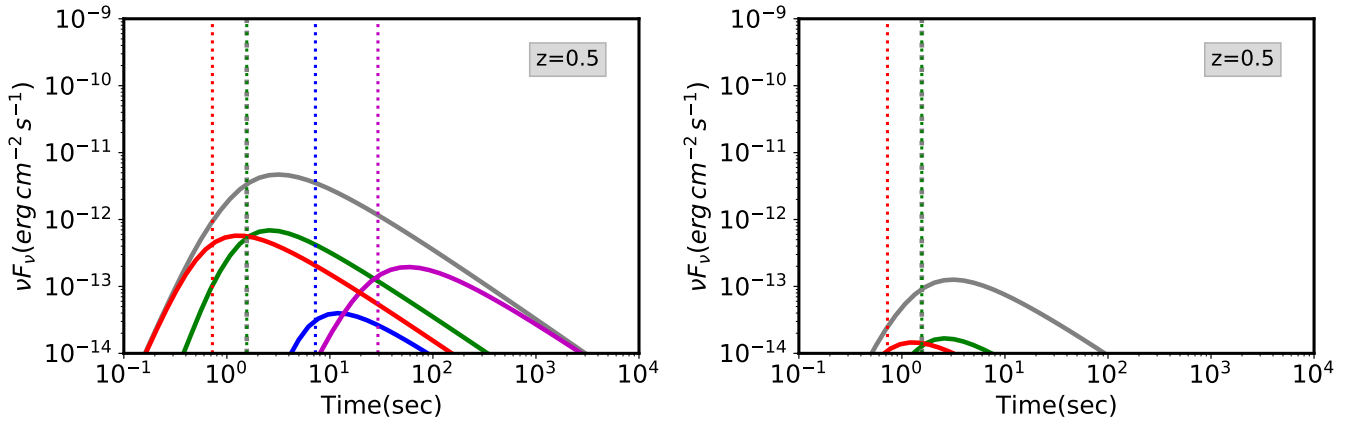


Figure 4. SSC Flux as a function of time is plotted for the same combination of microphysical parameters with a similar colour scheme as mentioned in figure-3, at the same fixed parameters with different redshift value at $z = 0.5$. The lightcurve plot of the left-side panel represents SSC Flux without EBL correction, and the right-side panel depicts the SSC flux with EBL correction by EBL Dominguez factor = 0.0233 at 500 GeV.

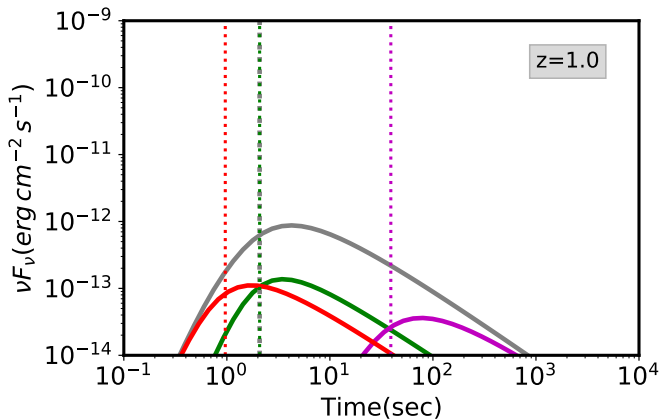


Figure 5. The lightcurve represents SSC Flux without EBL correction. With EBL Dominguez factor = 0.00012, at 500 GeV for $z = 1.0$, the EBL corrected SSC flux is going below the value of $10^{-14}\text{erg cm}^{-2} \text{s}^{-1}$, which is beyond the reach of CTA. Hence, the EBL corrected plot is discarded.

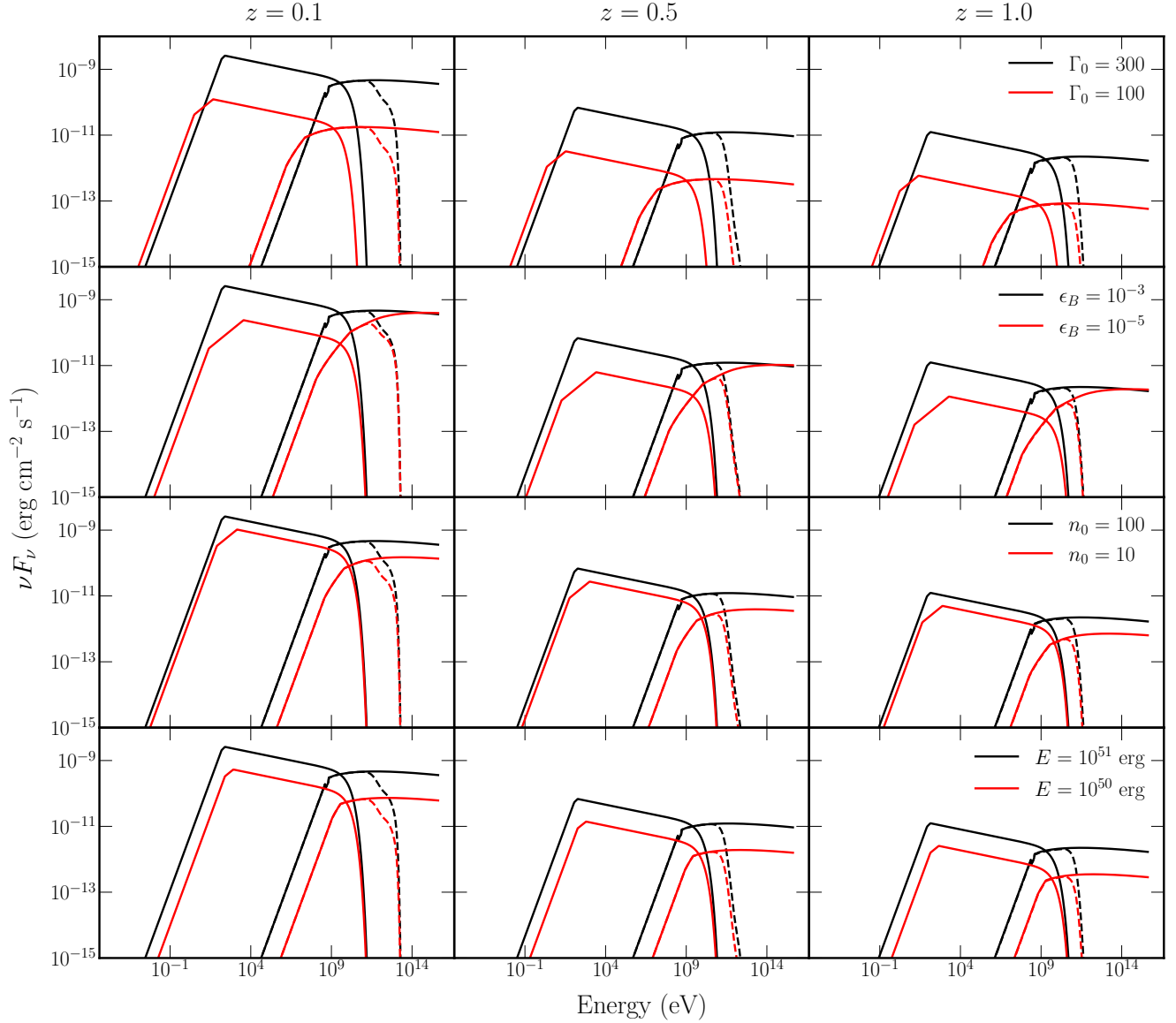


Figure 6. This shows the SEDs for different parameters and redshifts. From left to right column redshift values are $z = 0.1, 0.5$ and 1.0 . The first row depicts the plots with fixed $E = 10^{51}$ erg, $n_0 = 100$, $\epsilon_B = 10^{-5}$. For this row the black line represents $\Gamma_0 = 300$ and red line is for $\Gamma_0 = 100$. For the second row, $E = 10^{51}$ erg, $n_0 = 100$, $\Gamma_0 = 300$ are fixed, $\epsilon_B = 10^{-3}$ is the black line and $\epsilon_B = 10^{-5}$ is the red line. In third row, $E = 10^{51}$ erg, $\epsilon_B = 10^{-3}$, $\Gamma_0 = 300$ are fixed, $n_0 = 100$ and $n_0 = 10$ are black and red lines respectively. For fourth row, $n_0 = 100$, $\epsilon_B = 10^{-3}$, $\Gamma_0 = 300$ are fixed, $E = 10^{51}$ erg and $E = 10^{50}$ erg correspond to black and red lines respectively. All the solid lines represent flux without EBL corrections, whereas, the dashed lines represent the flux after EBL corrections.

Rhodes L., et al., 2020, *Monthly Notices of the Royal Astronomical Society*, 496, 3326

Rybicki G. B., 2004, *Radiative Processes in Astrophysics*. Wiley-VCH, doi:10.1002/9783527618170

Sari R., Esin A. A., 2001, *The Astrophysical Journal*, 548, 787–799

Sari R., Piran T., Narayan R., 1998, *Astrophys. J. Lett.*, 497, L17

Service A. T., 1986, *ApJ*, 307, 60

Stecker F. W., de Jager O. C., Salamon M. H., 1992, *ApJL*, 390

Tang Q.-W., Tam P.-H. T., Wang X.-Y., 2014, *ApJ*, 788, 156

Thompson C., 1994, *Monthly Notices of the Royal Astronomical Society*, 270, 480

Tramacere A., 2020, *Astrophysics Source Code Library*, pp ascl–2009

Tramacere A., Giommi P., Perri M., Verrecchia F., Tosti G., 2009, *Astronomy & Astrophysics*, 501, 879

Tramacere A., Massaro E., Taylor A., 2011, *The Astrophysical Journal*, 739,

66

Usov V., 1992, *The Astrophysical Journal*, 389, 635

Veres P., et al., 2019, *Nature*, 575, 459

Vurm I., Beloborodov A. M., 2017, *ApJ*, 846, 152

Wang X.-Y., He H.-N., Li Z., Wu X.-F., Dai Z.-G., 2010, *ApJ*, 712, 1232

Wang X.-Y., Liu R.-Y., Zhang H.-M., Xi S.-Q., Zhang B., 2019, *ApJ*, 884, 117

Wijers R., Galama T., 1999, *The Astrophysical Journal*, 523, 177

Woolsey S., 1993, in *Bulletin of the American Astronomical Society*, p. 894

Woolsey S., Bloom J., 2006, *Annu. Rev. Astron. Astrophys.*, 44, 507

Xue R. R., Tam P. H., Wagner S. J., Behera B., Fan Y. Z., Wei D. M., 2009, *ApJ*, 703, 60

Zhang B., 2018, *The Physics of Gamma-Ray Bursts*, doi:10.1017/9781139226530.

Zhang H., Christie I., Petropoulou M., Rueda-Becerril J. M., Giannios D.,

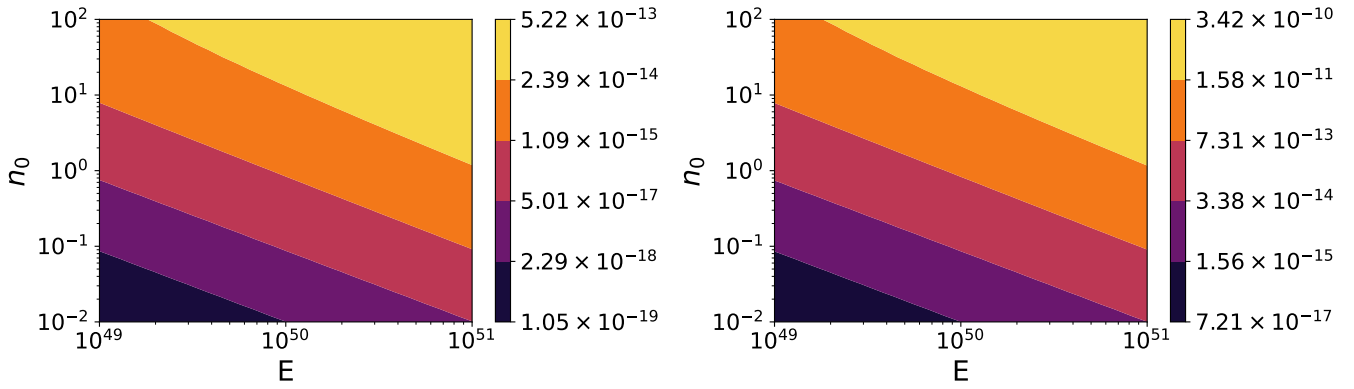


Figure 7. These plots depict the EBL corrected SSC peak flux for different E and n_0 values, with other parameters fixed as $\epsilon_e = 0.02$, $\epsilon_B = 0.001$, $\Gamma_0 = 300$. The left and right panels are for redshift $z = 0.5$ and $z = 0.1$ respectively.

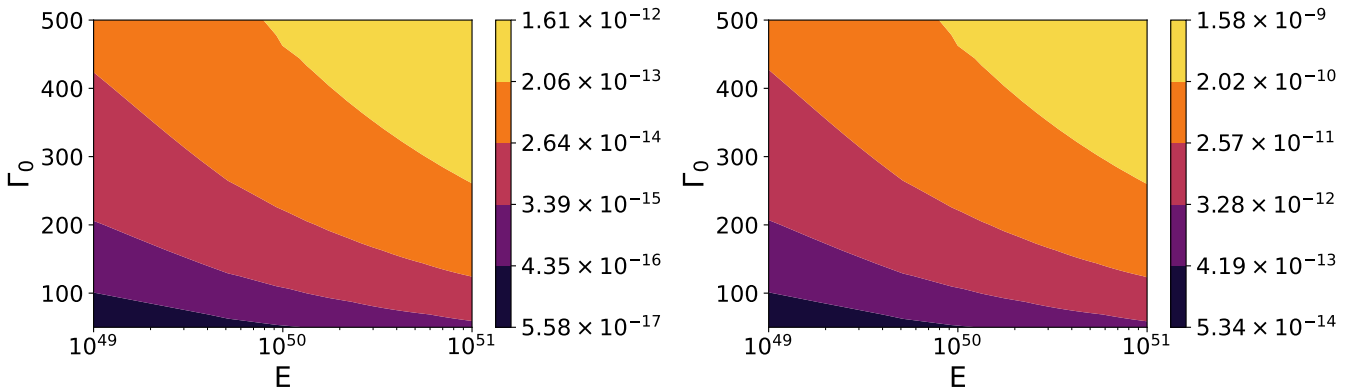


Figure 8. These plots show the EBL corrected SSC peak flux for different E and Γ_0 values, with other parameters fixed as $\epsilon_e = 0.02$, $\epsilon_B = 0.001$, $n_0 = 100$. The left panel and right panels are for redshift $z = 0.5$ and $z = 0.1$, respectively.

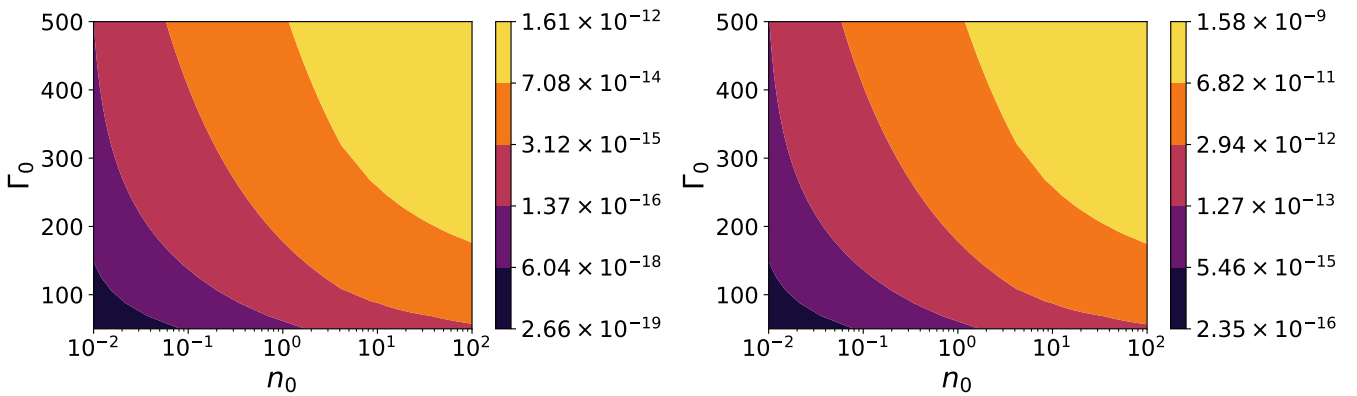


Figure 9. These plots show the EBL corrected SSC peak flux for different n_0 and Γ_0 values, with other parameters fixed as $\epsilon_e = 0.02$, $\epsilon_B = 0.001$, $E = 10^{51}$ erg. The left and right panels are for redshift $z = 0.5$ and $z = 0.1$, respectively.

2020a, Monthly Notices of the Royal Astronomical Society, 496, 974
 Zhang H., Christie I. M., Petropoulou M., Rueda-Becerril J. M., Giannios D.,
 2020b, *MNRAS*, 496, 974
 de Ugarte Postigo A., et al., 2022, GRB Coordinates Network, 32648, 1
 van Paradijs J., et al., 1997, *Nature*, 386, 686

This paper has been typeset from a \LaTeX file prepared by the author.

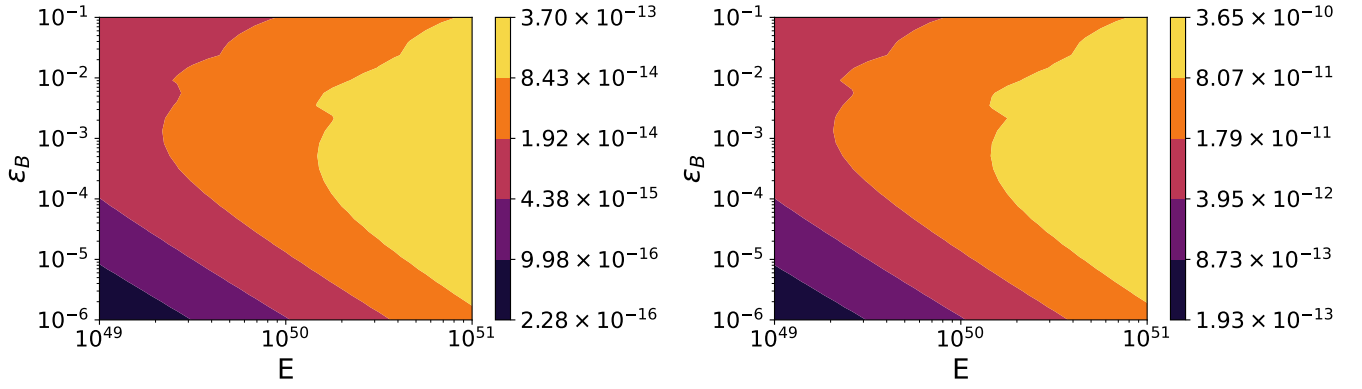


Figure 10. These plots show the EBL corrected SSC peak flux for different E and ϵ_B values, with other parameters fixed as $\epsilon_e = 0.02$, $n_0 = 100$, $\Gamma_0 = 300$. The left and right panels are for redshift $z = 0.5$ and $z = 0.1$, respectively.

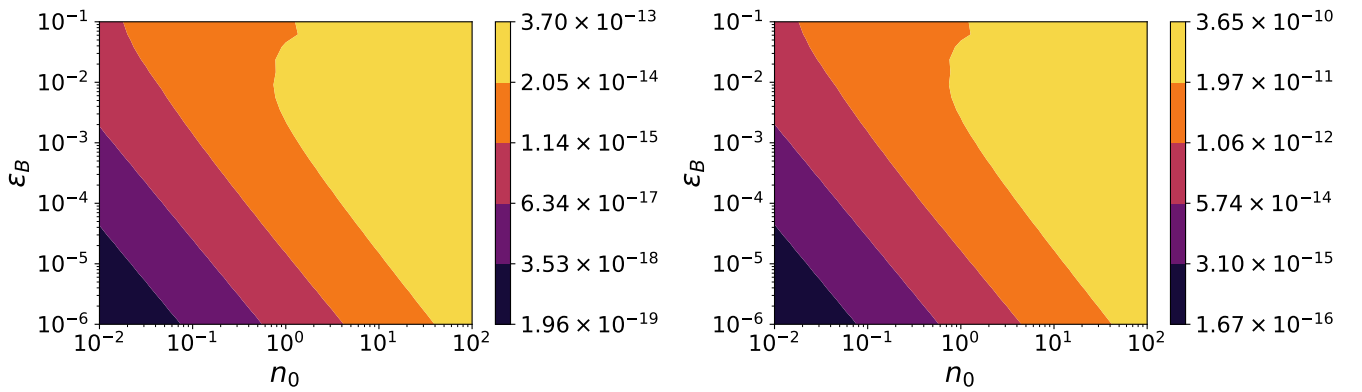


Figure 11. These plots show the EBL corrected SSC peak flux for different n_0 and ϵ_B values, with other parameters fixed as $\epsilon_e = 0.02$, $\Gamma_0 = 300$, $E = 10^{51}$ erg. The left and right panels are for redshift $z = 0.5$ and $z = 0.1$, respectively.